

# Self-Assembled Nanofibrous Hydrogels with Tunable Porous Network for Highly Efficient Solar Desalination in Strong Brine

Hao Li, Weixin Zhang, Jiawei Liu, Mingze Sun, Li Wang, and Lizhi Xu\*

Hydrogel-based solar evaporators (HSEs) emerged as energy-efficient designs for water purification due to the reduced vaporization enthalpy in the hydrated polymeric network. However, it remains challenging for HSEs to achieve stable performance in desalination, partly due to the tradeoff between desired evaporation dynamics and salt tolerance. Here, composite hydrogels with tunable self-assembled nanofiber networks are exploited for the engineering of solar evaporators with both high evaporation performance and resistance to salt accumulation. The nanofibrous hydrogel solar evaporators (NHSEs) present an intrinsic open network with high porosity, above 90%, enabling continuous water channels for efficient mass transfer. Theoretical modeling captures the complex nexus between microstructures and evaporation performance by coupling water transfer, thermal conduction, and vaporization enthalpy during evaporation. The mechanistic understanding and engineering tuning of the composites lead to an optimum configuration of NHSEs, which demonstrate a stable evaporation rate of  $2.85 \text{ kg m}^{-2} \text{ h}^{-1}$  during continuous desalination in 20% brine. The outstanding performance of NHSEs and the underlying design principles may facilitate further development of practical desalination systems.

## 1. Introduction

Solar evaporation is a promising approach to desalination due to its simple system configuration and high energy efficiency.<sup>[1,2]</sup> Extensive research efforts were recently invested into novel materials and structures for enhanced performance in solar desalination.<sup>[3–9]</sup> Among the variety of designs, hydrogels attracted wide attention due to their 3D hydrophilic networks that facilitate water replenishment and accelerate vapor generation via interactions with water molecules.<sup>[10–13]</sup> However, most of the reported hydrogel-based solar evaporators (HSEs) can stably operate only with low salinity liquid (<10%), which does not satisfy the requirements for industrial application or prolonged use.<sup>[14,15]</sup> Salt accumulation in HSEs often occurs during continuous evaporation especially in strong brine, which compromises the photothermal evaporation process by blocking water transport and solar reception.<sup>[16–19]</sup>


Existing strategies for enhancing salt tolerance in HSEs include local crystallization,<sup>[18,20]</sup> ion rejection,<sup>[17,21]</sup> Janus design,<sup>[19,22]</sup> and back diffusion.<sup>[23–25]</sup> Among these approaches, promoting back diffusion of ions into the bulk water is advantageous since it aims to eliminate salt accumulation in HSEs with feasible structures. Engineered channels with low diffusive tortuosity were used for enhancing the required mass transfer. For instance, vertical aligned vessels were constructed in HSEs to accelerate back diffusion of ions via directional confinement of water path.<sup>[26,27]</sup> However, heat loss to the bulk water is also aggravated with the enhancement of water flux, which compromises evaporation efficiency. Vertical radiant structures were developed to address the above tradeoff,<sup>[28]</sup> but the complicated fabrication renders it suboptimal for practical implementation. Alternative approaches aim to build open porous structures by porosigen,<sup>[29,30]</sup> gas-blowing,<sup>[31,32]</sup> and foaming polymerization,<sup>[33,34]</sup> which also create highly continuous water channels. Nevertheless, sophisticated preparation process and relatively low porosity of these fabricated porous hydrogels may limit their practical utilization.

Indeed, achieving optimum photothermal evaporation requires engineering of various physical processes that are mutually dependent. Although considerable efforts have been devoted to decoupling the water transfer and heat conduc-

H. Li, W. Zhang, J. Liu, M. Sun, L. Xu  
Department of Mechanical Engineering  
The University of Hong Kong  
Hong Kong SAR 999077, P. R. China  
E-mail: xulizhi@hku.hk

W. Zhang, L. Xu  
Advanced Biomedical Instrumentation Centre Limited  
Hong Kong SAR 999077, P. R. China

L. Wang  
Department of Civil Engineering  
The University of Hong Kong  
Hong Kong SAR 999077, P. R. China

 The ORCID identification number(s) for the author(s) of this article can be found under <https://doi.org/10.1002/adfm.202308492>

© 2023 The Authors. Advanced Functional Materials published by Wiley-VCH GmbH. This is an open access article under the terms of the Creative Commons Attribution-NonCommercial License, which permits use, distribution and reproduction in any medium, provided the original work is properly cited and is not used for commercial purposes.

DOI: 10.1002/adfm.202308492

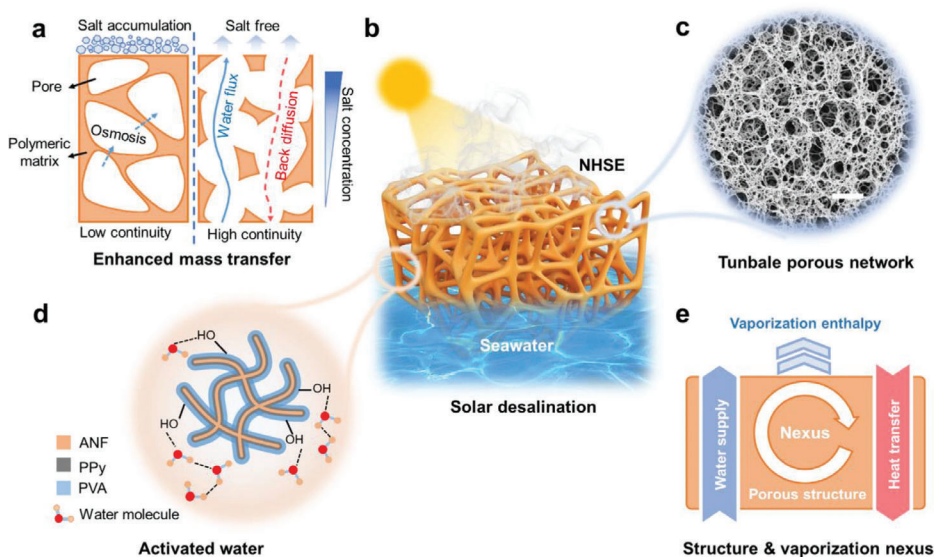


**Figure 1.** Solar desalination based on NHSE. a) Elimination of salt accumulation by enhancing mass transfer via highly continuous water channels. b) A schematic of solar desalination using NHSE. c) A scanning electron microscope (SEM) image showing the open porous network of NHSE. Scale bar: 2  $\mu\text{m}$ . d) A schematic illustrating the components of the hybrid nanofiber network with hydrophilic groups for water activation and PPy for photothermal conversion. e) A diagram illustration of the nexus between microstructure and vaporization performance, indicating the coupling of microstructure, water supply, heat transfer, and vaporization enthalpy.

tion in HSEs through regulating pore structures, the associated variation of vaporization enthalpy is usually overlooked, which actually affect the evaporation performance of HSEs.<sup>[25,35]</sup> Generally, the boosted water transfer by increasing porosity or pore diameter also results in an increase of vaporization enthalpy due to the weakened interaction between hydrophilic functional groups and water molecules, which is adverse to solar evaporation.<sup>[29]</sup> A labyrinth of nexus between microstructures, thermodynamics, and mass/heat transfer create difficulties for the optimization of HSEs. Careful designs regarding the complex interplay between physical processes are essential for achieving desired performance in solar evaporation.

We recently developed a series of porous composites based on aramid nanofibers (ANFs) with tunable microstructures and compositions, enabling a versatile platform for the engineering of functional hydrogels for solar desalination.<sup>[36,37]</sup> In the present work, we designed nanofibrous hydrogel solar evaporators (NHSEs) involving tunable open porous network to achieve high-performance solar desalination (Figure 1). The self-assembled network provides continuous microchannels for efficient mass transfer, thus preventing salt accumulation. It also presents abundant hydrophilic groups that facilitate water activation for reduced vaporization enthalpy, as well as uniformly loaded polypyrrole (PPy) for effective photothermal conversion. Through quantitative analysis on the interplay between various structural and thermodynamic parameters, in combination with rational experimental tuning, we identified a materials configuration showing stable evaporation rate of 2.85  $\text{kg m}^{-2} \text{h}^{-1}$  in 20% brine under solar illumination. The outstanding performance of NHSEs and the underlying design principles may provide insights for the development of advanced solar desalination systems.

## 2. Results and Discussion

The NHSEs were fabricated based on solution processing (Figure S1, Supporting Information). Specifically, ANFs and polyvinyl alcohol (PVA) were dispersed in dimethyl sulfoxide (DMSO) followed by mixing in the liquid phase. The incorporation of PVA provides extensive hydrophilic interface for water activation, and it toughens the fibrillar networks via hydrogen bonding with ANFs.<sup>[12,36,38]</sup> Solid hydrogels with open porous network were obtained by replacing DMSO with water. Tuning of porosity was achieved by varying the ANF and PVA contents in the hydrogels. Samples with high solid content (e.g.,  $\approx 12$  wt%) demonstrates hyperconnective nanofibrous networks ascribed to the high aspect ratio of ANFs and interfibrillar interactions (Figure 2a–c).<sup>[36,37]</sup> On the other hand, with the decrease of solid content (e.g., to  $\approx 3.9$  wt%), a hierarchical open porous structure started to form as ANFs aggregate into fiber bundles followed by assembly into a network at a higher length scale (Figure 2d,e and Figure S2, Supporting Information). The phenomenon is possibly induced by the extensive hydrogen bonding between fibrils and the energy minimum under low solid content. SEM images of a bulk sample indicate uniform distribution of ANF in the hydrogel (Figure S3, Supporting Information). A dependence of the pore size on the ANF concentration was observed (Figure S4, Supporting Information). Interactions between water molecules and the hydrophilic matrix are conducive to the reduction of vaporization enthalpy.<sup>[39]</sup> The water activation effect of hydrated polymeric network can be verified by Raman spectrum (Figure S11, Supporting Information). An ultralow vaporization enthalpy of 1050  $\text{J g}^{-1}$  was achieved by NHSEs (Figure S12, Supporting Information).

The resulting 3D networks exhibit pore sizes varying by  $\approx 10$  times (i.e., from 28 to 2491 nm) within a relatively narrow

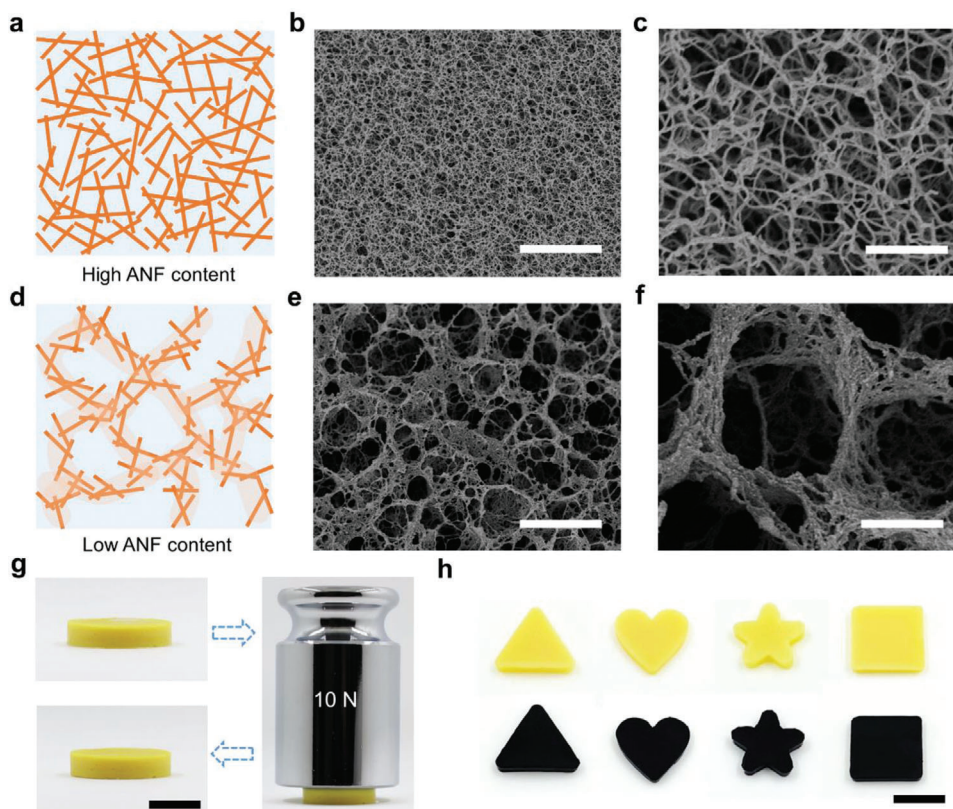


**Figure 2.** Structural characteristics of NHSEs. a) Schematic depiction of nanofiber network of NHSEs with high ANF content. b, c) SEM images of NHSEs with 2.5% ANF and 5% PVA. Scale bar: 5  $\mu\text{m}$  (b), 1  $\mu\text{m}$  (c). d) Schematic illustration of hierarchically porous network of NHSEs with low ANF content. e, f) SEM images of NHSEs with 0.5% ANF and 3.4% PVA. Scale bar: 5  $\mu\text{m}$  (e), 1  $\mu\text{m}$  (f). g) A sample of NHSE with and without a compressive load of 10 N. Scale bar: 1 cm. h) A photograph of NHSE samples molded into various shapes. Scale bar: 1 cm.

range of solid content ( $\approx 3.9\%$ – $10.9\%$ ), allowing for convenient tuning of transport properties. The high porosity ( $>90\%$ ) of the nanofiber hydrogels (Figure S5, Supporting Information) is conducive to the mass transfer as indicated by the equation of effective diffusion coefficient ( $D_{\text{eff}}$ ) in hydrogels:<sup>[40]</sup>

$$D_{\text{eff}} = \frac{D_0}{1 + p(1 - \epsilon)} \quad (1)$$

where  $D_0$  represents the bulk solution diffusion coefficient,  $p$  is the structure factor, and  $\epsilon$  is the porosity. In addition, the hyperconnective nanofiber network endows high structural stability and mechanical strength to the hydrogels (Figure 2g). The NHSEs were obtained by incorporating PPy as photothermal conversion material with ANF-PVA network. Notably, the PPy polymerizes along the nanofibers without compromising the porous structure of NHSE (Figure S6, Supporting Information), which is partly due to the  $\pi$ - $\pi$  stacking and hydrogen bonding between ANFs and PPy.<sup>[37]</sup> Due to the simple solution-based processing, NHSEs can be molded into various 3D shapes (Figure 2h and Figure S7, Supporting Information), allowing for flexible designs for evaporators.

Swelling experiments demonstrate excellent water transport properties of NHSEs. The swelling capacity of hydrogels can be obtained by measuring the water content ( $Q$ ):

$$Q = (W - W_d) / W_d \quad (2)$$

where  $W_d$  and  $W$  represent the weight of an aerogel sample prepared by critical point drying and the weight of corresponding hydrogel after hydration in water, respectively. The NHSEs present tunable saturated water content ( $Q_s$ ) ranging from 5.24 to 11.85  $\text{g g}^{-1}$  (Figure S8a, Supporting Information). Water transport rate  $V$  (Figure S8b, Supporting Information) can be estimated by an established formula:<sup>[10]</sup>

$$V = \frac{0.5Q_s}{t} \quad (3)$$

where  $t$  represents the half-swollen time. The water transport rate increases with increasing pore size, partly due to the lower tortuosity in hydrogel with larger pores (Figure 3b). A sharp increase of water transport rate occurred at hydrogel with 1.0% ANF and 6.6% PVA, which is ascribed to the formation of hierarchical structures and larger pores. The highest water transport rate of 1.38  $\text{g min}^{-1}$  was achieved by the sample with 0.7% ANF and 4.7% PVA (Figure 3b). As the ANF content drops below 1%, the ANF-PVA hydrogels demonstrated fast water transport superior to most of the reported HSEs (pore size  $\approx 100 \mu\text{m}$ ) for solar desalination (Figure 3c). With a similar pore size, the ANF-PVA hydrogels exhibit water absorption rate two orders of magnitude higher



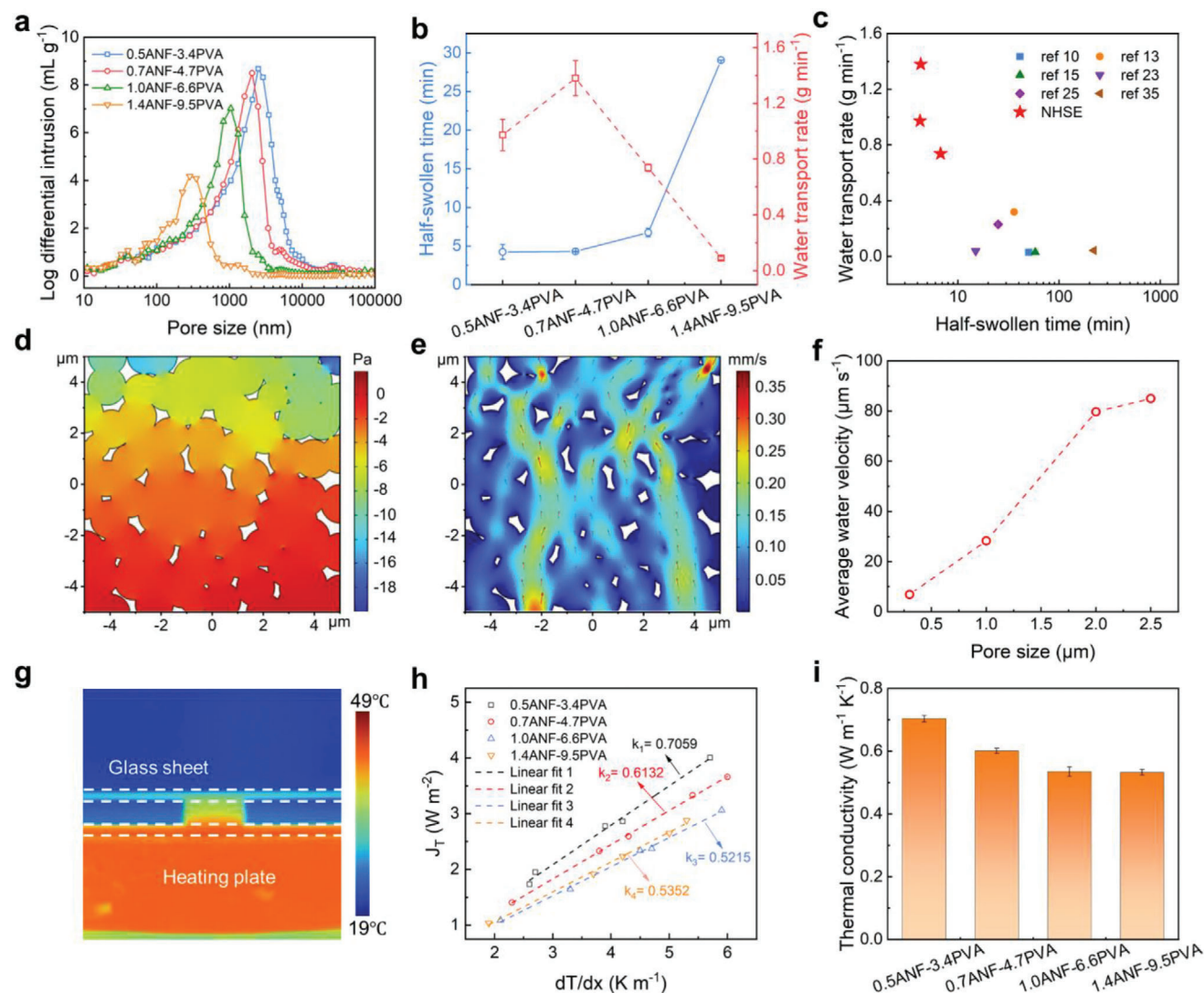


**Figure 3.** Water transfer and thermal behaviors of NHSEs. a) Pore size distribution of NHSEs. b) Half swollen time and calculated water transport rate of NHSEs. c) Comparison of half swollen time and water transport rate of NHSEs with other reported HSEs. d,e) Simulations of water pressure (d) and water velocity variation in microchannels (e). f) The simulated average water velocity in NHSEs with different pore sizes. g) Infrared image of NHSEs for the measurement of thermal conductivity. h,i) Calculation of thermal conductivity of different NHSEs.

than that of PVA hydrogels (Figure S9, Supporting Information), demonstrating the advantages of open microchannels in NHSE.

The effect of pore size on the water transport velocity was confirmed by numerical simulation. A computational model composed of overlapping circles was created in COMSOL to simulate the interconnected pores in NHSEs, where the diameter of the circle corresponds to the average pore size of the hydrogel. One sun illumination was applied at the upper boundary of the model for evaporation. The negative pressure on surface generated by evaporation combined with capillarity drives the water transport in microchannels (Figure 3d,e). The simulated water velocity in the microchannels increases as the pore size increases, which is consistent with the result obtained in the swelling experiments (Figure 3b,f).

The NHSEs also exhibit low thermal conductivity, which facilitates heat localization during solar desalination. Considering that

the NHSEs works in a hydrated state, measurement of thermal conductivity was conducted using hydrogels with saturated water content. The thermal conductivity of NHSEs decreases with decreasing pore size (Figure 3g,h), which is attributed to the increased thermal resistance by more interfaces and boundary effects with smaller pores. An ultralow thermal conductivity of 0.53 W m<sup>-1</sup> K<sup>-1</sup> is achieved by hydrogel with 1% ANF and 7.4% PVA. (Figure 3i). The PPy in NHSEs induces negligible deterioration on water transport and heat preservation (Figure S10, Supporting Information), further indicating the stability of the porous network.

Indeed, there is usually a tradeoff between efficient water transport and heat localization for effective photothermal evaporation. Furthermore, the variation of evaporation enthalpy originating from materials and microstructures may also present significant influences. Therefore, it is critically important to

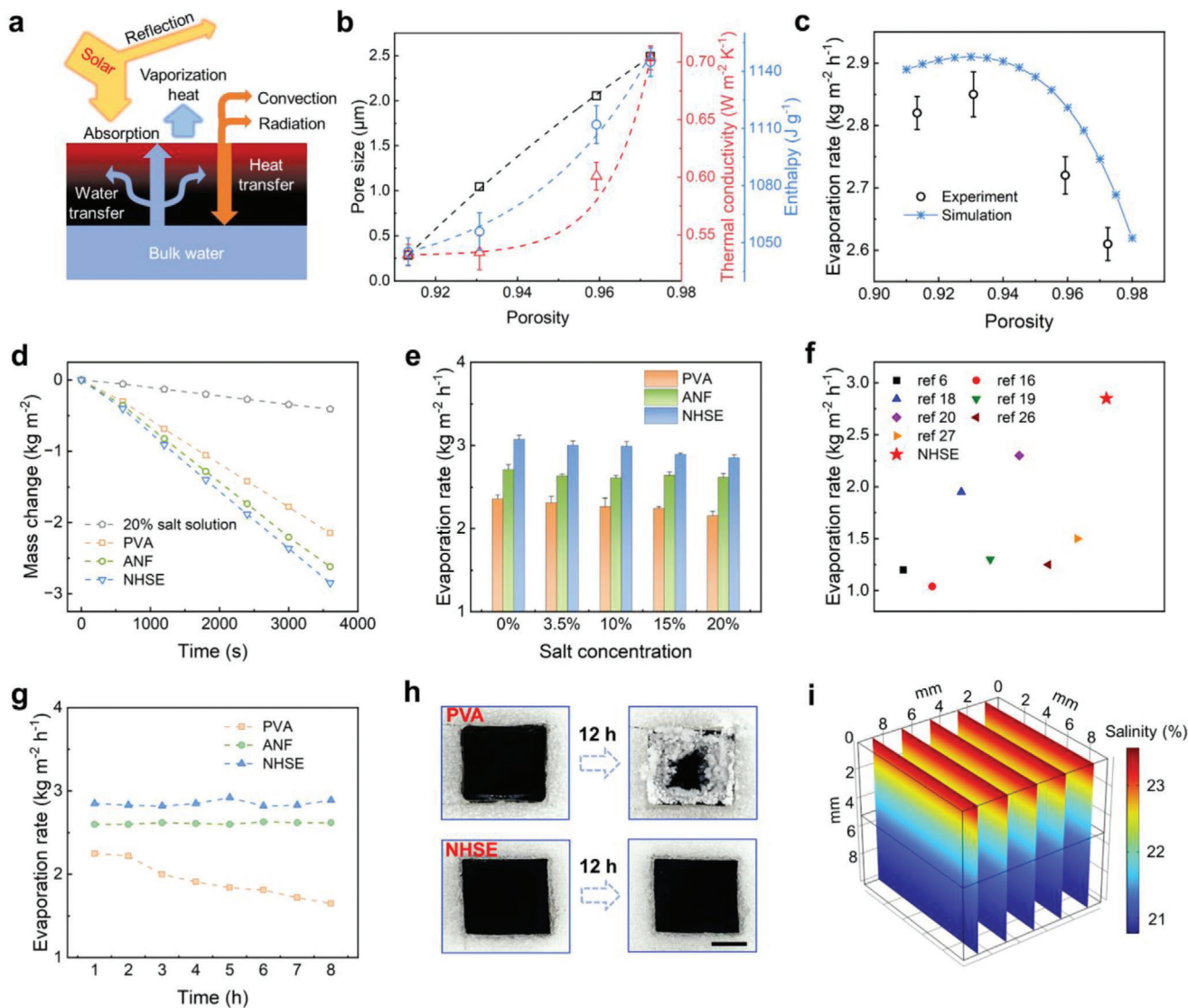


**Figure 4.** Engineering of solar desalination performances. a) The energy balance and mass transport in a solar desalination system. b) Experimental data (closed symbols) and fitted lines (dotted lines) of pore size, thermal conductivity, and vaporization enthalpy as a function of porosity. c) Experimental and simulated evaporation rate of NHSEs with various porosities. d) Evaporated water mass with various HSEs over 1 h under 1 sun illumination, with a 20% salt solution without evaporator as a control. e) Evaporation rates of different evaporators in various salt solutions under 1 sun. f) Solar evaporation rate of NHSE in 20% salt solution as compared with previous results reported in literature. g) Stability of different evaporators in 20% brine over 8 h of continuous evaporation. The evaporator based on PVA hydrogels exhibited an obvious decline in evaporation rate. h) Photographs of PVA hydrogel and NHSE with continuous evaporation in 20% brine for 12 h. Severe salt accumulation occurred on PVA hydrogel while no salt crystal appears on NHSE. Scale bar: 1 cm. i) Simulation of salt distribution in NHSEs during desalination in 20% brine under steady state.

understand the quantitative contributions of various structural, thermodynamic, and kinetic parameters to the evaporation performance for the engineering of NHSEs. To clarify the complex nexus between the physical processes, a computational model was developed based on the energy balance during solar evaporation (Figure 4a). The model was conducted by COMSOL Multiphysics 5.6, which coupled the heat transfer in porous media and the porous media flow into a stationary solver. All NHSEs were assumed with the same thermal convection and radiation to the environment (Equations (13) and (14)). Thermal insulation assumption was adopted as the boundary conditions of four

side faces due to the wrapped thermal insulation foam in the experiments (Figure S16, Supporting Information). The NHSEs demonstrated excellent solar absorbance above 98% as indicated by UV-vis-NIR spectra (Figure S13, Supporting Information), which was set as energy input efficiency of the evaporation system. Models of NHSEs were constructed based on the various porosity, pore size, vaporization enthalpy, and thermal conductivity. Quantitative relationships between the various parameters and porosity of NHSEs were fitted based on experimental data (Figure 4b, Equations (17)–(19)), which facilitate the calculation of evaporation rate as a function of porosity of NHSEs.

The simulation shows a maximum evaporation rate achieved by NHSEs with an intermediate porosity of 93%, which is consistent with the experimental observation (Figure 4c). These results can be understood from the coupling between vaporization enthalpy, water transfer, and heat localization of NHSEs during evaporation. On the one hand, NHSEs with lower porosity exhibit lower vaporization enthalpy and thermal conductivity, which facilitates evaporation. On the other hand, their smaller pores lead to less efficient water transfer, which might downgrade the evaporation performance. Indeed, the intermediate porosity associated with the maximum evaporation rate represents an optimum regarding these correlated processes. Simulations with independently controlled variables indicate further design principles for NHSEs (Figure S14, Supporting Information). Specifically, the evaporation performance is tightly correlated with the porosity (Figure S14a, Supporting Information) and vaporization enthalpy (Figure S14b, Supporting Information), which represent water transport and energy efficiency, respectively. However, the effect of thermal conductivity on the evaporation rate is relatively minor especially with pore sizes below 30  $\mu\text{m}$  (Figure S14c, Supporting Information). This result may be related to the limited fluid flow in small pores regardless of the differences in temperature field induced by various thermal conductivities. We note that our simulation is based on the constitutive relationships derived from macroscopic models, which may have limitations when investigating complex thermal hydraulic behaviors of mesoscopic porous media. Further development of microscopic models and examinations with other materials systems would be helpful for a complete mechanistic understanding.

The NHSE with 1% ANF and 6.6% PVA exhibited the best evaporation performance, which was utilized for the application of solar-driven desalination. Stable water transfer and thermal conductivity of NHSEs in various salt solutions (Figure S15, Supporting Information) indicate robust performances for treating brines. Evaporation performance of NHSEs was measured under one sun illumination using a custom testing device (Figure S16, Supporting Information). Compared with the pure ANF hydrogels and PVA hydrogels, NHSEs achieved evaporation rates 10%–30% higher (Figure 4c,d and Figure S17, Supporting Information), which is resulted from the combination of porous nanofiber network and hydrated polymer matrix. NHSEs demonstrate the lowest surface temperature among these evaporators (Figure S18, Supporting Information) due to the significant vaporization that takes away heat from the surface.<sup>[12]</sup> This low surface temperature facilitates the heat localization by minimizing the heat radiation to the environment. With brines with salinity ranging from 0% to 20%, the NHSE achieved high evaporation rate from 3.1 to 2.85  $\text{kg m}^{-2} \text{h}^{-1}$  (Figure 4d), and efficiency from 90% to 83% (Figure S19, Supporting Information), which outperforms most of the reported works for strong brine desalination (Figure 4f and Table S1, Supporting Information).

The open porous network of NHSEs enables efficient back diffusion of salt from evaporation surface to the bulk water, resulting in excellent salt-resistance. The desalination stabilities of various hydrogel evaporators were evaluated by conducting continuous evaporation in 20% brine (Figure 4g). Both NHSE and ANF hydrogels demonstrated stable evaporation, verifying the efficient mass transfer in 3D nanofibrous network. In contrast, a decline of evaporation rate was observed in PVA hydrogels af-

ter 2 h of evaporation. Severe salt accumulation occurred at the surface of PVA hydrogel after 12 h of continuous evaporation in 20% brine, while no salt crystals appeared on NHSE (Figure 4h). Additionally, the PVA hydrogel evaporator suffered a dramatic shrinkage at the evaporating interface during the solar desalination (Figure S20a, Supporting Information), prompted by the mismatch between water supply and vaporization. Continuous evaporation concentrates the salt solution in the water channels, which may lead to deswelling of polymeric matrix driven by osmotic pressure. This phenomenon is represented by the shrinkage of PVA hydrogel in 20% brine (Figure S20d, Supporting Information). The shrinkage further decreases the water transfer in the hydrogel, resulting in a vicious cycle. Inversely, the ANF network in NHSEs provides a rigid skeleton that prevents the shrinking effect and maintains the efficient water transfer in high-salinity brine during solar desalination (Figure S20b,c, Supporting Information). The efficient mass transfer enables self-generation of NHSE by dissolving salt crystals added on the surface (Figure S21, Supporting Information). Moreover, numerical simulations indicated that the steady-state salt concentration at evaporation surface of NHSE stays below the saturation level (Figure 4i and Figure S22, Supporting Information), which prevents salt crystallization. This property of NHSEs is beneficial for long-lasting solar desalination with strong brine.

We further characterized the quality of water treated by NHSEs (Figure S23, Supporting Information). The decrease of salinity is validated by the increased resistance of the water samples from kilohm to megohm (Figure 5a) via a multimeter with the fixed distance between two electrodes (Figure S24, Supporting Information). In addition to brine, NHSE can be used to purify acid and alkaline liquids. The purified water samples demonstrate pH values close to neutral (Figure 5b and Figure S25, Supporting Information). Moreover, we performed solar desalination using real seawater collected from Kennedy Town, Hong Kong. The concentrations of four typical elements ( $\text{Na}^+$ ,  $\text{Mg}^{2+}$ ,  $\text{K}^+$ ,  $\text{Ca}^{2+}$ ) in seawater decreased by approximately three orders of magnitude after purification, which meet the standards for drinking water set by the World Health Organization (Figure 5c). Liquid samples with colored containments were also purified, leading to colorless and transparent water as proved via the UV–vis spectra (Figure 5d). Furthermore, successful cell proliferation in the nutrient solution with the purified water as the solvent indicates the desired water purity (Figure 5e). An efficient water production of 10.4  $\text{kg m}^{-2} \text{d}^{-1}$  was achieved by NHSE in an outdoor evaporation experiment (Figure S26, Supporting Information), indicating the reliability of NHSE for practical applications.

### 3. Conclusion

In conclusion, we have developed composite nanofibrous hydrogels for solar desalination applicable in high-salinity brine. The efficient mass transfer, low thermal conductivity, and reduced vaporization enthalpy inherited from the hybrid nanofiber network are crucial for the efficient and stable performance in solar desalination. The mechanistic insights regarding the microstructural, thermodynamic, and kinetic processes and their quantitative contributions to the evaporation performance are conducive to the engineering of other HSEs. Developing mesoscopic models, such as those involving lattice Boltzmann method, would



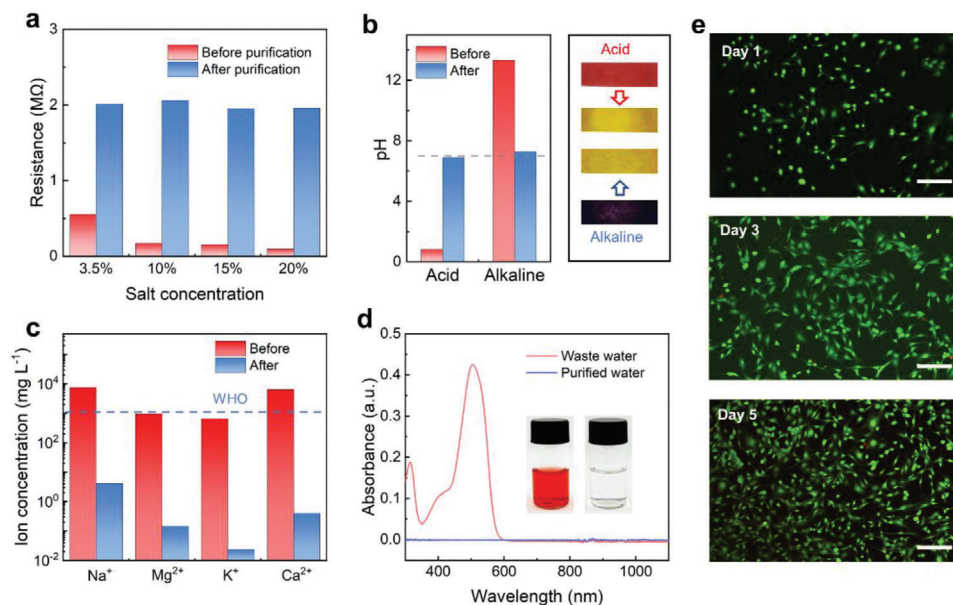


**Figure 5.** Water purification with NHSEs. a) Electrical resistance of various salt solutions before and after purification. b) Change in pH value of acid and alkaline solutions before and after purification. c) Concentrations of four primary ions ( $\text{Na}^+$ ,  $\text{Mg}^{2+}$ ,  $\text{K}^+$ ,  $\text{Ca}^{2+}$ ) in seawater, before and after desalination. The dotted line indicates the WHO standard for drinking water. d) UV-vis absorption spectra of dye-contaminated water and purified water. The inset presents photographs of water samples before and after purification. e) Proliferation of NIH 3T3 fibroblasts cultured with water purified by NHSEs. Scale bars: 200  $\mu\text{m}$ .

further advance the understanding of mass and heat transfer in the porous media.<sup>[41]</sup> In most cases, promoting hydration of the polymeric network by introducing appropriate functional groups would be helpful to lower vaporization enthalpy with minimal impact on the water transfer. Finally, device-level designs for solar evaporators would provide additional performance enhancement with improved efficiency in solar energy utilization.

## 4. Experimental Section

**Preparation of Hydrogels for Solar Evaporation:** ANF-PVA hydrogels were prepared using solvent exchange methods reported by previous work.<sup>[36]</sup> Briefly, ANF and PVA dispersion was prepared by dissolving Kevlar para-aramid pulp (Type 979; DuPont) and poly(vinyl alcohol) (PVA; Mn  $\approx$  75 000; hydrolysis degree of 96% $\approx$ 98%; Aladdin Reagent) in dimethyl sulfoxide (DMSO; Aladdin Reagent) under magnetic stirring at 95 °C for 7 days, respectively. The ANF (1.5%) and PVA (10%) dispersion were mixed up with the ratio of 1:1, followed by poured into a mold. The hydrogels were obtained after exchanging DMSO with deionized (DI) water completely. Solid content of the hydrogel was regulated by diluting the ANF/PVA mixture with DMSO or evaporating excess DMSO in vacuum oven. No volume change occurred in all NHSEs after solvent exchange.

PVA hydrogels were prepared using freeze-thaw method. Typically, 0.5 mg mL<sup>-1</sup> of PVA aqueous solution was poured into a mold then frozen in the refrigerator at -24 °C. Thereafter, the frozen mixture was thawed at room temperature. PVA hydrogels were obtained after five freeze-thaw cycles.

For the coating of PPy, the hydrogels were soaked with 0.5 M  $\text{FeCl}_3$  (Sigma-Aldrich) solution. Then the hydrogels were exposed to pyrrole (Sigma-Aldrich) vapor at 4 °C for 10 min. After polymerization, the hydrogels were washed with DI water to remove unreacted ions and pyrrole.

**Characterization:** The SEM images were obtained by scanning electron microscope (Hitachi S4800 FEG) after dried by critical point dryer (CPD; Tousimis Autosamdri 931). Pore size distribution was character-

ized by mercury intrusion porosimeter (MIP, AutoPore IV 9500). Absorption spectra of hydrogels and liquids were conducted using UV-vis-NIR spectrometer (UV 3600I plus, Shimadzu) and UV-vis adsorption spectra (UV-2600, Shimadzu), respectively. Ohmic resistance and pH value of water samples were tested by a digital multimeter (Victor, VC890C) and a pH meter (Mettler Toledo, FiveEasy), respectively. Ion concentration was measured by inductively coupled plasma mass spectrometry (ICP-MS, ELAN DRC-e, Perkin Elmer).

The porosity ( $\epsilon$ ) of samples was calculated by:

$$\epsilon = \left( 1 - \frac{11.5\rho_0}{1.5\rho_a + 10\rho_p} \right) \times 100\% \quad (4)$$

where  $\rho_0$ ,  $\rho_a$ , and  $\rho_p$  represent the density of the bulk sample, ANF (1.44 g cm<sup>-3</sup>), and PVA (1.19 g cm<sup>-3</sup>), respectively. The coefficients in the equation refer to the ratio of ANF and PVA (1.5:10) in hydrogel.

**Solar Vapor Generation Experiments:** The hydrogel evaporator with size of 1 cm  $\times$  1 cm  $\times$  0.5 cm was floated on the water for purification with the assistance of polyethylene foam. A solar simulator (Aulight, CEL-S500-T5) was used to provide continuous one sun illumination. The solar intensity on the evaporator surface was measured using a solar power meter (Tenmars, TM-207). The mass change of the evaporation device was measured using an electronic balance (Mettler Toledo) after stabilization under one sun for 0.5 h. An infrared camera (Fluke Ti480) was used to record the temperature change of the evaporator. All the evaporation tests were conducted at room temperature (25 °C) with the relative humidity of 45%.

**Swelling Behavior of NHSEs:** Water transport rate of the hydrogels were measured by evaluating their swelling behaviors. A CPD dried hydrogel with the size of 1 cm  $\times$  1 cm  $\times$  0.5 cm was immersed in the pure water or salt solutions at 30 °C to monitor the weight change until fully swollen (no weight change in 0.5 h). Specially, the samples were wiped by air-laid paper to remove the water in capillary channels before each measurement.

**Evaluation of Thermal Conductivity:** Thermal conductivities of hydrogels were measured according to Fourier's law. The hydrogel with the size of 1 cm  $\times$  1 cm  $\times$  0.3 cm was sandwiched between two 1 mm glass plates with the conductivity of 1.3 W m<sup>-1</sup> K<sup>-1</sup>. The sandwich was heated at

different temperatures on a heating plate to record the steady-state temperatures at interfaces (heating plate-bottom glass, bottom glass-hydrogel, and hydrogel-top glass) of the sandwich using thermocouples. Assuming that the glass plate and hydrogels have similar heat fluxes, the thermal conductivities of hydrogels were calculated by:<sup>[42]</sup>

$$J_T = -k \frac{dT}{dx} \quad (5)$$

where  $J_T$  is the heat flux per unit area,  $k$  is the thermal conductivity of the material, and  $dT/dx$  is the temperature gradient at the heat transfer direction.

**Calculation of Equivalent Vaporization Enthalpy and Efficiency:** Equivalent vaporization enthalpies of hydrogels were obtained by measuring the evaporation rates of samples in the dark condition.<sup>[12]</sup> Water and hydrogels with the same evaporation area were placed in the same dark environment at 25 °C and 45% of humidity for 24 h to ensure the same energy input ( $U_{in}$ ). The equivalent vaporization enthalpy was obtained by:

$$U_{in} = h_0 m_0 = h_{eq} m \quad (6)$$

where  $h_0$  is the enthalpy of pure water ( $\approx 2450 \text{ J g}^{-1}$ ),  $m_0$  is the mass loss of water,  $m$  is the mass decline of hydrogel, and  $h_{eq}$  is the equivalent vaporization enthalpy of the hydrogel, respectively.

Evaporation efficiencies are calculated by the equation as below:

$$\eta = \frac{\dot{m} h_{eq}}{C_{opt} q_i} \quad (7)$$

where  $\eta$  represents the evaporation efficiency,  $\dot{m}$  is the evaporation rate,  $h_{eq}$  is the equivalent enthalpy,  $C_{opt}$  is the optical concentration, and  $q_i$  is the solar irradiation power.

**Numerical Simulation:** The commercial software COMSOL Multiphysics v5.6 was used to simulate the water transfer, evaporation flux, and salt distribution of NHSEs.

A model was constructed for simulation analysis of water velocity in microchannels. The interconnected pores were represented by overlapping circles with various diameters corresponding to the average pore sizes of different NHSEs. A constant solar irradiation of  $1 \text{ kW m}^{-2}$  was applied to the top surface for driving evaporation. The water flux entered the evaporator equals to the escaped water flux caused by evaporation. Considering the water confinement of the capillary channels, the water transport was simulated by solving the following equations:

$$\rho (u \times \nabla) u = \nabla \times (-pI + \mu (\nabla u + (\nabla u)^T)) + F + \rho g \quad (8)$$

$$\rho \nabla \times u = 0 \quad (9)$$

where the  $\rho$  and  $\mu$  are the mass density and viscosity of water.  $u$ ,  $p$ , and  $T$  represent the fluid flow speed, pressure, and temperature of water, respectively.  $I$  and  $F$  are the second order unit tensor and gravity of water, respectively.

The simulation of solar evaporation considers vaporization enthalpy, heat transfer, and water transport in NHSEs. The 3D domain ( $1 \text{ cm} \times 1 \text{ cm} \times 0.5 \text{ cm}$ ) referred to the size of NHSE was discretized with a mesh consisting of up to 20 000 tetrahedron-dominant elements. The heat transfer in solar evaporator follows the equations as below:

$$\rho C_{p,tot} u \times \nabla T + \nabla \times q = Q + Q_{evap} + Q_c + Q_e \quad (10)$$

$$q = -k_{eff} \nabla T \quad (11)$$

$$Q_{evap} = -h_{evap} \dot{m} \quad (12)$$

$$Q_c = -h_c (T - T_e) \quad (13)$$

$$Q_e = -E_m \sigma (T^4 - T_e^4) \quad (14)$$

$$Q = \alpha q_i \quad (15)$$

where  $\rho$  is the density,  $C_{p,tot}$  is the total heat capacity at constant pressure,  $q$  is the conductive heat flux,  $k_{eff}$  is the effective thermal conductivity,  $u$  is the velocity field,  $Q_{evap}$  is the latent heat source in NHSE,  $h_{evap}$  is the vaporization enthalpy,  $\dot{m}$  is the evaporation flux on the evaporating surface,  $Q_c$  is the heat convection on the surface,  $h_c$  is the convection coefficient ( $10 \text{ W m}^{-2} \text{ K}^{-1}$ ),  $Q_e$  is the heat radiation on the surface,  $E_m$  is the surface emissivity (0.9),  $\sigma$  is the Stefan-Boltzmann constant ( $5.67 \times 10^{-8} \text{ W m}^{-2} \text{ K}^{-4}$ ),  $T_e$  is the environment temperature (298.15 K),  $Q$  is the energy input on the top surface of evaporator,  $q_i$  is the solar intensity ( $1 \text{ kW m}^{-2}$ ) applied to the evaporator, and  $\alpha$  is the solar absorptance efficiency (98%) of NHSE.

As the water evaporation comes from the difference between the mass concentration of the evaporating surface and the air, the  $\dot{m}$  can be calculated as below:<sup>[43]</sup>

$$\dot{m} = -k_m \frac{M}{R} \left( \frac{p_w^{v,sat}}{T} - H_R \frac{p_e^{v,sat}}{T_e} \right) \quad (16)$$

where  $M$  represents the molar mass of water ( $18 \times 10^{-3} \text{ kg mol}^{-1}$ ),  $R$  is the universal gas constant ( $8.314 \text{ J mol}^{-1} \text{ K}^{-1}$ ),  $p_w^{v,sat}$  and  $p_e^{v,sat}$  are the pressures of water vapor at the surface temperature ( $T$ ) and at the environment temperature ( $T_e$ ), respectively,  $H_R$  is the relative humidity (45%), and  $k_m$  is the convective mass transfer coefficient ( $0.01 \text{ m s}^{-1}$ ).

The variation of thermal conductivity ( $k_{eff}$ ), pore size ( $R_c$ ), and vaporization enthalpy ( $h_{evap}$ ) as the function of porosity ( $\epsilon$ ) were obtained by fitting the experimental data (Figure 4b):

$$k_{eff} = 0.532 + 2.834 \times 10^{-4} \left( e^{\frac{-0.913}{0.009}} + e^{\frac{-0.913}{0.011}} \right) \left[ \text{W m}^{-2} \text{ K}^{-1} \right] \quad (17)$$

$$R_c = -579.249 + 588.425 \left( 1 - e^{-\frac{\epsilon}{0.218}} \right) \left[ \mu\text{m} \right] \quad (18)$$

$$h_{evap} = 1027.432 + 8.875 \left( e^{\frac{-0.913}{0.0282}} + e^{\frac{-0.913}{0.0344}} \right) \left[ \text{J g}^{-1} \right] \quad (19)$$

To simulate the salt distribution in NHSEs, a mass flux of NaCl ( $J_{evap}$ ) was applied on the desalination interface:<sup>[44]</sup>

$$J_{evap} = \frac{q'_{evap} \cdot c}{h_{evap} \rho} \quad (20)$$

$$\rho(c, T) = \rho_0(T) + \beta \cdot c \quad (21)$$

where  $q'_{evap}$  represents the evaporation heat flux on the surface,  $c$  is the brine concentration,  $h_{evap}$  is the latent heat at the desalination interface,  $\rho$  is the brine density, which is affected by the brine concentration and temperature, and  $\beta$  ( $0.033 \text{ kg mol}^{-1}$ ) is a proportionality constant. The salt concentration at the bottom of NHSEs was set as the 3.5%–20%.

## Supporting Information

Supporting Information is available from the Wiley Online Library or from the author.

## Acknowledgements

L.X. acknowledges funding support from Research Grants Council (RGC) (Project 17200320, 17200722, 17201523 and C6004-22Y), Environment and Conservation Fund (project 125/2021) and The University of Hong Kong (Seed Funding for Strategic Interdisciplinary Research Scheme 102010174). This work was also supported by the Health@InnoHK program of the Innovation and Technology Commission of the Hong Kong SAR Government.



## Conflict of Interest

The authors declare no conflict of interest.

## Data Availability Statement

The data that support the findings of this study are available from the corresponding author upon reasonable request.

## Keywords

hydrogel evaporators, nanofiber networks, salt resistance, solar desalination, structure-performance nexus

Received: July 21, 2023

Revised: August 16, 2023

Published online:

- 
- [1] L. Zhou, Y. Tan, J. Wang, W. Xu, Y. Yuan, W. Cai, S. Zhu, J. Zhu, *Nat. Photonics* **2016**, *10*, 393.
- [2] E. Chiavazzo, M. Morciano, F. Viglino, M. Fasano, P. Asinari, *Nat. Sustain.* **2018**, *1*, 763.
- [3] P. Tao, G. Ni, C. Song, W. Shang, J. Wu, J. Zhu, G. Chen, T. Deng, *Nat. Energy* **2018**, *3*, 1031.
- [4] L. Wu, Z. Dong, Z. Cai, T. Ganapathy, N. X. Fang, C. Li, C. Yu, Y. Zhang, Y. Song, *Nat. Commun.* **2020**, *11*, 521.
- [5] Y. Guo, H. Lu, F. Zhao, X. Zhou, W. Shi, G. Yu, *Adv. Mater.* **2020**, *32*, 1907061.
- [6] X. Chen, S. He, M. M. Falinski, Y. Wang, T. Li, S. Zheng, D. Sun, J. Dai, Y. Bian, X. Zhu, J. Jiang, L. Hu, Z. J. Ren, *Energy Environ. Sci.* **2021**, *14*, 5347.
- [7] N. Li, K. Shao, J. He, S. Wang, S. Li, X. Wu, J. Li, C. Guo, L. Yu, P. Murto, J. Chen, X. Xu, *Small* **2023**, *19*, 2301474.
- [8] N. Li, L. Qiao, J. He, S. Wang, L. Yu, P. Murto, X. Li, X. Xu, *Adv. Funct. Mater.* **2021**, *31*, 2008681.
- [9] F. Li, N. Li, S. Wang, L. Qiao, L. Yu, P. Murto, X. Xu, *Adv. Funct. Mater.* **2021**, *31*, 2104464.
- [10] X. Zhou, F. Zhao, Y. Guo, Y. Zhang, G. Yu, *Energy Environ. Sci.* **2018**, *11*, 1985.
- [11] Y. Guo, G. Yu, *Acc. Mater. Res.* **2021**, *2*, 374.
- [12] F. Zhao, X. Zhou, Y. Shi, X. Qian, M. Alexander, X. Zhao, S. Mendez, R. Yang, L. Qu, G. Yu, *Nat. Nanotechnol.* **2018**, *13*, 489.
- [13] X. Zhou, F. Zhao, Y. Guo, B. Rosenberger, G. Yu, *Sci. Adv.* **2019**, *5*, eaaw5484.
- [14] J. Zeng, Q. Wang, Y. Shi, P. Liu, R. Chen, *Adv. Energy Mater.* **2019**, *9*, 1900552.
- [15] M. Tan, J. Wang, W. Song, J. Fang, X. Zhang, *J. Mater. Chem. A* **2019**, *7*, 1244.
- [16] Y. Kuang, C. Chen, S. He, E. M. Hitz, Y. Wang, W. Gan, R. Mi, L. Hu, *Adv. Mater.* **2019**, *31*, 1900498.
- [17] W. Zhao, H. Gong, Y. Song, B. Li, N. Xu, X. Min, G. Liu, B. Zhu, L. Zhou, X.-X. Zhang, J. Zhu, *Adv. Funct. Mater.* **2021**, *31*, 2100025.
- [18] L. Li, N. He, B. Jiang, K. Yu, Q. Zhang, H. Zhang, D. Tang, Y. Song, *Adv. Funct. Mater.* **2021**, *31*, 2104380.
- [19] W. Xu, X. Hu, S. Zhuang, Y. Wang, X. Li, L. Zhou, S. Zhu, J. Zhu, *Adv. Energy Mater.* **2018**, *8*, 1702884.
- [20] Z. Wang, J. Gao, J. Zhou, J. Gong, L. Shang, H. Ye, F. He, S. Peng, Z. Lin, Y. Li, F. Caruso, *Adv. Mater.* **2023**, *35*, 2209015.
- [21] N. He, Y. Yang, H. Wang, F. Li, B. Jiang, D. Tang, L. Li, *Adv. Mater.* **2023**, *35*, 2300189.
- [22] C. Ma, Q. Liu, Q. Peng, G. Yang, M. Jiang, L. Zong, J. Zhang, *ACS Nano* **2021**, *15*, 19877.
- [23] W. Tu, Z. Wang, Q. Wu, H. Huang, Y. Liu, M. Shao, B. Yao, Z. Kang, *J. Mater. Chem. A* **2020**, *8*, 10260.
- [24] H. Yang, Y. Sun, M. Peng, M. Cai, B. Zhao, D. Li, Z. Liang, L. Jiang, *ACS Nano* **2022**, *16*, 2511.
- [25] H. Zou, X. Meng, X. Zhao, J. Qiu, *Adv. Mater.* **2023**, *35*, 2207262.
- [26] X. Dong, Y. Si, C. Chen, B. Ding, H. Deng, *ACS Nano* **2021**, *15*, 12256.
- [27] X. Dong, L. Cao, Y. Si, B. Ding, H. Deng, *Adv. Mater.* **2020**, *32*, 1908269.
- [28] X. Liu, F. Chen, Y. Li, H. Jiang, D. D. Mishra, F. Yu, Z. Chen, C. Hu, Y. Chen, L. Qu, *Adv. Mater.* **2022**, *34*, 2203137.
- [29] Y. Guo, L. S. de Vasconcelos, N. Manohar, J. Geng, K. P. Johnston, G. Yu, *Angew. Chem., Int. Ed.* **2022**, *61*, e202114074.
- [30] J. Jiang, H. Jiang, Y. Xu, L. Ai, *Desalination* **2022**, *539*, 115943.
- [31] T. Xu, Y. Xu, J. Wang, H. Lu, W. Liu, J. Wang, *Chem. Eng. J.* **2021**, *415*, 128893.
- [32] J. Li, L. Yan, X. Li, W. Song, Y. Li, *J. Environ. Chem. Eng.* **2022**, *10*, 107690.
- [33] X. Chen, Z. Wu, D. Lai, M. Zheng, L. Xu, J. Huo, Z. Chen, B. Yuan, M.-L. Fu, *J. Mater. Chem. A* **2020**, *8*, 22645.
- [34] P. Liu, Y.-b. Hu, X.-Y. Li, L. Xu, C. Chen, B. Yuan, M.-L. Fu, *Angew. Chem., Int. Ed.* **2022**, *61*, e202208587.
- [35] X. Zhou, Y. Guo, F. Zhao, W. Shi, G. Yu, *Adv. Mater.* **2020**, *32*, 2007012.
- [36] L. Xu, X. Zhao, C. Xu, N. A. Kotov, *Adv. Mater.* **2018**, *30*, 1703343.
- [37] H. He, H. Li, A. Pu, W. Li, K. Ban, L. Xu, *Nat. Commun.* **2023**, *14*, 759.
- [38] H. Liu, H. Li, Z. Wang, X. Wei, H. Zhu, M. Sun, Y. Lin, L. Xu, *Adv. Mater.* **2022**, *34*, 2207350.
- [39] B. Luo, J. Wen, H. Wang, S. Zheng, R. Liao, W. Chen, O. Mahian, X. Li, *Energy Environ. Mater.* **2023**, *6*, e12353.
- [40] Y. Alsaïd, S. Wu, D. Wu, Y. Du, L. Shi, R. Khodambashi, R. Rico, M. Hua, Y. Yan, Y. Zhao, D. Aukes, X. He, *Adv. Mater.* **2021**, *33*, 2008235.
- [41] S. Chen, G. D. Doolen, *Annu. Rev. Fluid Mech.* **1998**, *30*, 329.
- [42] H. Wang, R. Zhang, D. Yuan, S. Xu, L. Wang, *Adv. Funct. Mater.* **2020**, *30*, 2003995.
- [43] R. Fillet, V. Nicolas, V. Fierro, A. Celzard, *Int. J. Heat Mass Transfer* **2021**, *181*, 121852.
- [44] L. Zhang, X. Li, Y. Zhong, A. Leroy, Z. Xu, L. Zhao, E. N. Wang, *Nat. Commun.* **2022**, *13*, 849.